PCCP

PAPER

View Article Online
View Journal | View Issue

Cite this: *Phys. Chem. Chem. Phys.*, 2025, **27**, 23030

How the $n_{Nu} \rightarrow \sigma^*_{C-Cl}$ hyperconjugation interaction affects intrinsic reactivity in an S_N2 reaction

Leonardo Saravia F.,[a] Jorge Gutiérrez-Flores,[b] Eduardo H. Huerta,*[a] Jorge Garza,[b] Rubicelia Vargas*[b] and Marcos Hernández-Rodriguez*[a]

Hyperconjugative interactions are widely recognized as stabilizing electronic effects in molecular systems. While their involvement in chemical transformations has been suggested, it remains as an open question whether their influence pertains to thermodynamic stabilization or if they directly affect intrinsic kinetic parameters (also referred to as the intrinsic activation barrier). In this work, we address a fundamental question: can $n_{Nu} \rightarrow \sigma^*_{C-Cl}$ hyperconjugation directly shape the intrinsic barrier in an asymmetric S_N2 reaction? To explore this, we present a systematic computational study using the MP2-SMD(THF)/cc-pVTZ level of theory, evaluating how $n_{Nu} \rightarrow \sigma^*_{C-Cl}$ interactions influence the intrinsic activation barrier in reactions of the type Y^- + CH_3–Cl. It is worth noting that energy differences were also evaluated using the CCSD(T)-SMD(THF) method. Intrinsic barriers were extracted from the theoretical activation barrier using Marcus' theory to isolate the required energy for the nuclear reorganization free from thermodynamic bias. The donor–acceptor interactions were quantified through natural bond orbital (NBO) analysis; moreover, quantum theory of atoms in molecules (QTAIM) descriptors provided a complementary, orbital-independent perspective. In the studied systems, a strong correlation between the $E^{(2)}_{n\rightarrow\sigma^*}$ stabilization energies and the intrinsic activation barriers was observed, one that is not evident when considering apparent barriers. This distinction underscores, within the present framework, the importance of isolating intrinsic contributions when evaluating fundamental reactivity trends. QTAIM descriptors, such as the electron density at the bond critical point (ρ_{BCP}) and the $|V_{BCP}|/G_{BCP}$ ratio, captured aspects of the local electronic environment, particularly electronegativity and polarizability, that were consistent with the intrinsic reactivity observed across the specific nucleophile families examined. In systems bearing α-substituents, the presence of secondary stabilizing interactions, likely involving non-covalent contacts between the nucleophile and C–H bonds of the electrophile, may contribute to lowering the intrinsic barrier. Together, these findings demonstrate that both NBO and QTAIM analyses are robust tools to determine the electronic contributions that govern reactivity and selectivity in the analyzed S_N2 reactions. Furthermore, they position hyperconjugation not merely as a passive stabilizing effect but also as an active modulator capable of tuning intrinsic reactivity in organic reactions.

Received 3rd July 2025,
Accepted 26th September 2025

DOI: 10.1039/d5cp02545a

rsc.li/pccp

1 Introduction

Hyperconjugation represents one of the most subtle orbital interactions yet decisive in organic chemistry, with wide-ranging implications from conformational stability to chemical reactivity.[1] This quantum mechanical phenomenon can arise from the electron delocalization between (1) a filled σ orbital and an adjacent empty p or π* antibonding orbital; (2) a lone pair (in a non-bonding orbital) or a π-bonding orbital and a σ* antibonding orbital; or (3) two σ orbitals, one bonding and the other antibonding, allowing for electron density redistribution across space. The efficiency of this interaction is strongly dependent on a molecular geometry that favors appropriate orbital overlap.[2,3] Among the many well-documented examples that demonstrate the presence of stabilizing hyperconjugative interactions (HypI), two notable cases are: (1) the conformational preference in ethane (Fig. 1a), where computational

[a] *Instituto de Química, Universidad Nacional Autónoma de México, Circuito Exterior, Ciudad Universitaria, Alcaldía Coyoacán C.P. 04510, Ciudad de México, Mexico. E-mail: e.hh@quimica.unam.mx, marcoshr@unam.mx*
[b] *Departamento de Química, División de Ciencias Básicas e Ingeniería, Universidad Autónoma Metropolitana Iztapalapa, San Rafael Atlixco 186, Col. Vicentina, C.P. 09340, Iztapalapa, CDMX, Mexico. E-mail: rvargas@izt.uam.mx*

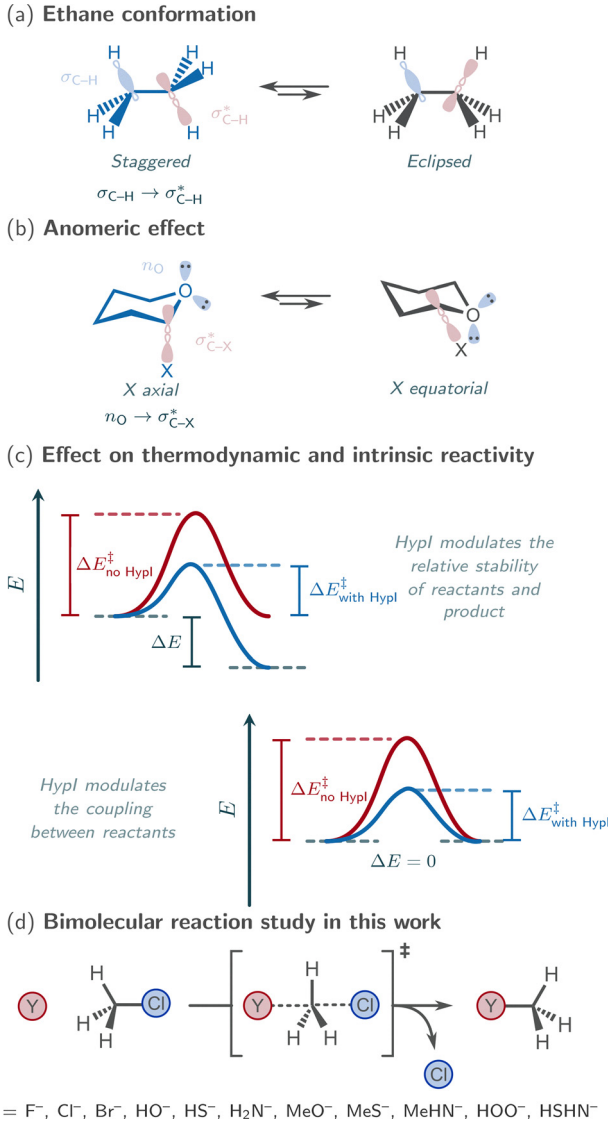

Fig. 1 (a) and (b) Representative configurational processes stabilized by hyperconjugative interactions (Hypl); the most stable conformers are highlighted in blue. (c) Conceptual illustration of how hyperconjugation can modulate both thermodynamic parameters (*e.g.*, reaction energies) and intrinsic barriers. (d) Schematic representation of the S_N2 reaction under investigation, including the series of nucleophiles considered in this study.

studies have shown that the staggered conformation is stabilized by interactions between adjacent σ_{C-H} and σ^*_{C-H} orbitals;[4–6] and (2) the well-known anomeric effect in heterocycles (*e.g.*, 2-heteroatom substituted tetrahydropyran, Fig. 1b),[7–9] where the preference for the axial orientation of the heteroatom substituent X at the anomeric carbon has been attributed to the antiperiplanar disposition of the axial lone pair of the endocyclic oxygen and the C–X bond which enables the delocalization of electrons to the antibonding orbital C–X by hyperconjugation $n_O \rightarrow \sigma^*_{C-X}$.[10,11] It is worth noting that, in both cases, complementary interpretations have also been proposed, such as steric repulsion in ethane conformation and electrostatic effects in the anomeric effect, highlighting the multifactorial nature of these phenomena.[12,13]

Beyond its structural role, hyperconjugation raises fundamental questions about its influence in chemical reactivity and selectivity, particularly through its potential to modulate the energy barriers that govern molecular transformations, a phenomenon supported by various mechanistic studies across distinct reaction types.[14–16] These questions naturally lead to analyzing the relationship between kinetic and thermodynamic parameters in chemical reactions, an essential aspect of physical organic chemistry. To address this issue, several theoretical models have been proposed to decompose the activation energy, also known as observable or apparent activation energy, ($\Delta E^{\ddagger}$), into conceptually distinct components: a thermodynamic term dependent on the reaction energy (ΔE), defined as the energy difference between reactants and products; and an intrinsic barrier ($\Delta E^{\ddagger}_0$), which reflects the energetic cost (associated with nuclear reorganization during the chemical transformation) of an idealized isoenergetic transformation ($\Delta E = 0$), and consequently depends on the chemical nature of the interacting species. Within this framework, models such as the Bell–Evans–Polanyi model[17–19] and its extension by Laffler[20] describe the activation energy as a linear function of the reaction energy, $\Delta E^{\ddagger} = \Delta E^{\ddagger}_0 + \alpha\Delta E$, where $\Delta E^{\ddagger}_0$ (intercept) and α (Brønsted slope) are treated as intrinsic properties characteristic of each reaction family. However, when ΔE varies significantly, such linear approximations become inadequate, and more general formulations, such as Marcus' theory, are required. Marcus' theory introduces a quadratic dependence and systematically separates thermodynamic effects from purely structural and, therefore, electronic factors.[21] Originally developed to describe classical electron transfer processes, this framework has proven particularly effective in rationalizing a wide range of organic reactions where thermodynamic and kinetic factors are tightly coupled.[22–24]

In this context, it is worth considering how certain intrinsic electronic factors, particularly those related to the local organization of electron density, may contribute to the intrinsic barrier itself. Among these contributions, hyperconjugation emerges as an outstanding candidate whose influence may extend beyond the thermodynamic stabilization of reactants or products to actively modulate the energy profile of the reaction (Fig. 1c).[25–29] If such influence on the intrinsic barrier is confirmed, hyperconjugation would cease to be viewed merely as a passive stabilizing factor and instead be recognized as a determinant of reactivity and selectivity in organic systems.

As a model system to investigate the influence of electronic interactions on molecular reactivity, this work presents a theoretical study of the bimolecular nucleophilic substitution (S_N2) reaction. Beyond its classical role as a mechanistic paradigm in physical organic chemistry, the S_N2 reaction remains a subject of ongoing research due to its synthetic utility and the emergence of new mechanistic questions and conceptual approaches.[30–36] Its well-defined mechanistic framework allows for a meaningful dissection of both thermodynamic and intrinsic contributions to the activation barrier, making it a powerful

platform for probing fundamental reactivity principles. This process makes it an ideal model to evaluate how specific electronic interactions, particularly hyperconjugation of the type n → σ*, can influence these distinct energetic components (thermodynamic and intrinsic barriers). We hypothesize that such interactions not only stabilize the involved stationary states, but also lower the intrinsic barrier itself, thereby acting as a key electronic determinant of reactivity. Our theoretical modeling considers the interactions between a series of 11 nucleophiles with chloromethane as a model electrophile to test this hypothesis (Fig. 1d). Analysis of these systems will allow us to establish a relationship between the strength of hyperconjugative interactions and intrinsic barriers, offering quantitative insight into the direct impact of hyperconjugation on reactivity. Despite the numerous elegantly designed quantum chemical studies that have furthered our understanding of the S_N2 cornerstone reaction,[37–39] to the best of our knowledge, no systematic analysis has been conducted to quantify the influence of specific electronic interactions, such as n → σ* hyperconjugation, on the intrinsic barrier $\Delta E_0^{\ddagger}$ in reactions of the type $Y^- + CH_3$–Cl. Most studies have focused on identity reactions, $X^- + CH_3$–X,[40–42] which limits the ability to assess and highlight the role of thermodynamic contributions in modulating reactivity. The knowledge generated in this work will not only offer tools for a deeper understanding of chemical transformations but will also position hyperconjugation as an additional electronic degree of freedom for the rational design of more reactive substrates and the precise modulation of reactivity and selectivity in organic transformations.

2 Computational details and models

Quantum chemical calculations were performed using the Gaussian16 software package.[43] Geometry optimizations of all stationary points, including reactants, products, and transition states, were carried out at the MP2 level of theory[44–49] combined with Dunning's cc-pVTZ basis set[50–52] (MP2/cc-pVTZ). Solvent effects were included with the continuum solvent model (CSM) approached through SMD formulation,[53] using tetrahydrofuran (THF) as the solvent. This choice provided a suitable balance between the computational cost and accuracy,[54] while enabling meaningful correlations between activation barriers and reaction exothermicity.[55,56] THF is an aprotic ubiquitous solvent in organic synthesis which preserves nucleophilicity trends comparable to those observed in the gas phase,[57–60] making it particularly appropriate for the analysis of intrinsic electronic effects such as hyperconjugation. All optimized structures were characterized through vibrational frequency analysis: local energy minima exhibited only real frequencies, whereas transition states were confirmed by the presence of a single imaginary frequency. Gibbs free energies were computed at 298.15 K and 1 atm. To test the correlation effects incorporated by the MP2 method, in this article, the CCSD(T) method was considered over geometries optimized at the MP2 level. Generally, the lack of correlation effects in the Hartree–Fock method (HF) is evident when its results are compared with those obtained from MP2 and CCSD(T) methods.

The direct influence of thermodynamic factors on activation barriers can be evaluated through Marcus' theory,[61–65] which decomposes the activation energy ($\Delta E^{\ddagger}$) into two components: an intrinsic activation barrier ($\Delta_0 E^{\ddagger}$) and a thermodynamic contribution (ΔE). The intrinsic barrier represents the minimum energy required to reach the transition state under thermoneutral conditions, reflecting the total cost of nuclear reorganization. The thermodynamic term reflects the driving force based on the relative stability between reactants and products. Within this framework, the activation energy increases when the reaction energy (ΔE) is positive and decreases when ΔE is negative. Assuming that the potential energy surfaces of reactants and products can be approximated by parabolas, the activation energy is given using the following classical Marcus expression:[61,66]

$$\Delta E^{\ddagger} = \Delta_0 E^{\ddagger} + \frac{\Delta E}{2} + \frac{\Delta E^2}{16\Delta_0 E^{\ddagger}} \quad (1)$$

Furthermore, when both the activation and reaction energies are known (either experimentally or computationally), the intrinsic barrier can be estimated by solving eqn (1) for $\Delta_0 E^{\ddagger}$, yielding the modified form:

$$\Delta_0 E^{\ddagger} = \frac{1}{2}\left[\Delta E^{\ddagger} - \frac{1}{2}\Delta E + \sqrt{\left[\Delta E^{\ddagger}\right]^2 - \Delta E^{\ddagger}\Delta E}\right] \quad (2)$$

This alternative formulation (eqn (2)) will be particularly useful because it allows a direct comparison between $\Delta_0 E^{\ddagger}$ of S_N2 reactions with different $\Delta E \neq 0$ (free from thermodynamic bias) and hyperconjugative interactions.

Two complementary approaches were employed to reveal key electronic aspects of the reaction to interpret intrinsic barriers: natural bond orbital (NBO) analysis[67–75] and topological analysis of the electron density based on the quantum theory of atoms in molecules (QTAIM).[76]

NBO analysis has emerged as a valuable theoretical framework for rationalizing reactivity trends in S_N2 reactions, particularly in cases where activation barriers deviate from classical expected patterns based on nucleophilicity, leaving group ability, or steric effects associated with substituents on the electrophilic carbon.[77–80] This analysis provides a quantitative estimate of the electronic stabilization arising from donor–acceptor interactions, particularly those involving the transfer of electron density from a filled (donor) orbital to an empty or antibonding (acceptor) orbital. This stabilization is estimated using second-order perturbation theory:

$$E^{(2)} = -n_i \frac{(F_{ij})^2}{\varepsilon_j - \varepsilon_i} \quad (3)$$

where n_i is the occupancy of the donor orbital i (typically close to 2), ε_i and ε_j are the orbital energies, and F_{ij} is the Fock matrix element coupling orbitals i and j.[72] Therefore, the strength of the donor–acceptor interaction depends on donor occupancy, the energy gap, and a non-zero Fock matrix element. The resulting stabilization is independent of the orbital phase, since the

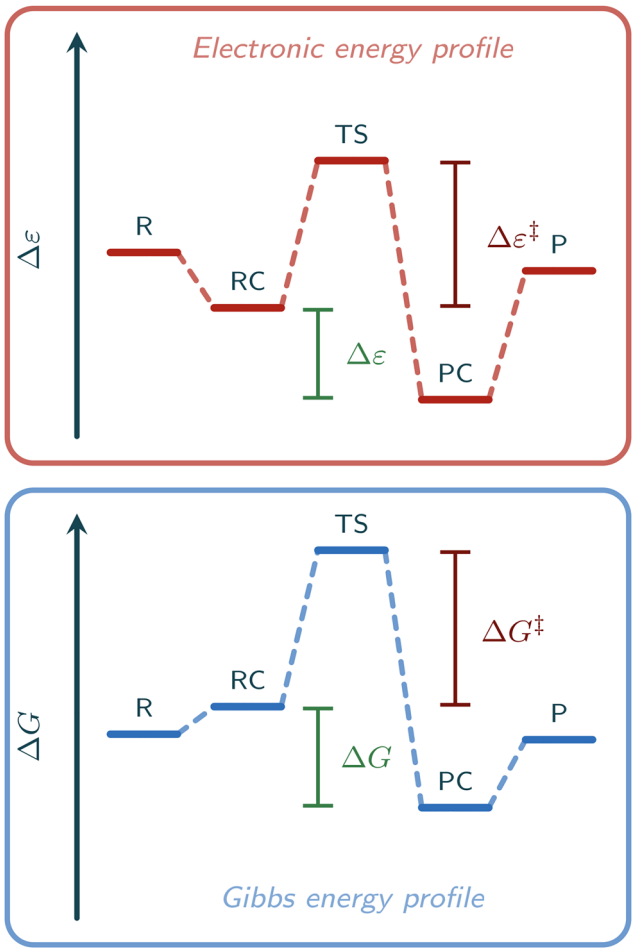

Fig. 2 Electronic (red, left) and Gibbs free energy (blue, right) profiles for the S_N2 reaction. Vertical lines point out the stationary states used for calculating barriers ($\Delta\varepsilon^{\ddagger}$ and $\Delta G^{\ddagger}$) and reaction energies ($\Delta\varepsilon$ and ΔG), the latter obtained from the energy difference between intermediates involved in the rate-determining step of the reaction.

perturbation expression involves the square of the coupling term ($F_{ij} = \langle i|\hat{F}|j\rangle$ in eqn (3), where $\hat{F}$ is Fock's operator), which remains unchanged under a change of orbital sign.[75] In this study, the donor orbital corresponds to the n_{Nu} lone pair on the nucleophile. In contrast, the acceptor orbital is the antibonding orbital of the electrophilic C–Cl bond, σ^{*}_{C-Cl}.

QTAIM analysis, on the other hand, relies on the topological characterization of the electron density $\rho(\vec{r})$, identifying critical points (CPs) where its gradient vanishes ($\nabla\rho(\vec{r}) = 0$), and bond paths (BPs), which represent trajectories of maximum electron density connecting pairs of nuclei. CPs are classified by their topological index ranges and curvature (ω, σ); of particular interest in this study are bond critical points (BCPs), characterized as (3, −1), which indicate interactions between two nuclei, such as those between the nucleophile and the electrophile. The sign of the Laplacian of the electron density at the BCP, $\nabla^2\rho(\vec{r})$, determines whether the interaction is shared-shell (covalent) if negative, or closed-shell (non-covalent) if positive. In addition, Espinosa *et al.*[81] proposed that $|V_{BCP}|/G_{BCP}$, the ratio between the magnitude of the potential energy density and the kinetic energy density at the BCP, acts as a local energetic descriptor of the stabilization/delocalization balance. According to this criterion, an interaction is closed-shell if $|V_{BCP}|/G_{BCP} < 1$, partially covalent if $1 < |V_{BCP}|/G_{BCP} < 2$, and shared-shell if $|V_{BCP}|/G_{BCP} > 2$. This parameter thus identifies the threshold beyond which an interaction becomes energetically stabilizing, associated with local density accumulation and the possible bond formation. Furthermore, this method offers an orbital-independent description based on the real-space charge distribution, enabling the inference of the physical nature of the interactions involved in S_N2 reactions.[33]

Together, these descriptors offer a robust basis for correlating electronic and orbital contributions with intrinsic activation barriers and understanding the nature of the nucleophilic interaction from both energetic and structural perspectives. NBO analysis was performed using the Gaussian16 implementation (NBO v3), while QTAIM calculations were carried out with the GPUAM software.[82–84]

3 Results and discussion

3.1 Activation energy profile

The first step in assessing the role of hyperconjugation in the bimolecular nucleophilic substitution (S_N2) reaction was to determine whether thermodynamic or intrinsic factors predominantly govern the activation barriers. To this end, barriers and reaction energies were calculated for a representative series of nucleophiles, using chloromethane as the model electrophile. Fig. 2 shows a schematic energy profile illustrating the key chemical species involved in the process without corresponding to any specific system. Both electronic energies (red, top) and Gibbs free energies (blue, bottom) are displayed, providing a clear visualization of the energy evolution from reactants to products. Five relevant states of the mechanism are identified: reactants (R), reactant complex (RC), transition state (TS), product complex (PC), and products (P). The relative energy values of these intermediates are provided in Table S1 of the SI, where all energies are reported regarding the reactants as a reference. Throughout the following discussion, ε and G denote the electronic energy and Gibbs free energy, respectively.

Before analyzing activation barriers and reaction energies, the relative stability of the intermediate complexes, specifically the reactant and product complexes, was examined based on their relative electronic energies (Table S1). In the halide nucleophile series, the RC stability followed the order F^- (−4.7 kcal mol^{-1}) > Br^- (−2.7 kcal mol^{-1}) > Cl^- (7.2 kcal mol^{-1}), a trend that remained consistent in the product complexes: F^- (−28.2 kcal mol^{-1}) > Br^- (−4.4 kcal mol^{-1}) > Cl^- (7.2 kcal mol^{-1}). For Cl^-, both RC and PC stabilities are the same because this process corresponds to an identity reaction. For simple nucleophiles (H_2N^-, HO^-, and HS^-) and their substituted counterparts ($MeHN^-$, MeO^-, and MeS^-), the oxygen-containing RCs were more stable than their nitrogen- and sulfur-based analogues. In contrast, the trend reversed for the

Table 1 Activation barriers and reaction energies (kcal mol^{-1}) for the S_N2 reaction of chloromethane with various nucleophiles, reported as electronic energies (ε) at MP2, CCSD(T), and HF levels and Gibbs free energies (G) at the MP2 level

	MP2[a]		MP2[a]		CCSD(T)[b]		HF[c]	
Nu	$\Delta\varepsilon^{\ddagger}(1)$	$\Delta\varepsilon(1)$	$\Delta G^{\ddagger}(1)$	$\Delta G(1)$	$\Delta\varepsilon^{\ddagger}(2)$	$\Delta\varepsilon(2)$	$\Delta\varepsilon^{\ddagger}(3)$	$\Delta\varepsilon(3)$
Halide nucleophiles								
F^-	10.9	−23.5	13.2	−21.7	9.4	−25.0	12.8	−30.2
Cl^-	20.6	0.0	21.8	0.3	19.4	0.0	23.0	0.0
Br^-	17.9	−1.8	19.2	−1.6	16.9	−1.5	21.2	0.0
Simple nucleophiles								
H_2N^-	5.9	−68.4	7.2	−64.9	5.1	−68.2	9.8	−77.2
HO^-	6.4	−54.3	7.2	−52.2	5.3	−55.3	5.6	−67.8
HS^-	14.4	−23.9	16.3	−22.4	13.7	−23.3	18.5	−26.2
Substituted nucleophiles								
CH_3HN^-	3.9	−72.9	5.8	−68.9	3.4	−72.4	9.0	−82.3
CH_3O^-	7.1	−50.0	6.3	−46.2	6.3	−50.5	7.8	−63.2
CH_3S^-	10.8	−34.3	11.9	−32.8	10.4	−33.4	15.8	−37.8
Nucleophiles with α-substituents								
HOO^-	4.1	−50.9	4.6	−49.7	3.2	−50.3	6.9	−56.7
$HSHN^-$	7.6	−54.5	10.6	−50.1	7.2	−54.2	11.5	−63.1

[a] MP2-SMD(THF)/cc-pVTZ. [b] CCSD(T)-SMD(THF)/cc-pVTZ//MP2-SMD(THF)/cc-pVTZ. [c] HF-SMD(THF)/cc-pVTZ//MP2-SMD(THF)/cc-pVTZ.

PCs: nitrogenated derivatives were the most stable, followed by the oxygenated and sulfur-based ones. Regarding nucleophiles with α-substituents, HOO^- was more stable (−7.6 kcal mol^{-1}) than $HSHN^-$ (−4.4 kcal mol^{-1}) in the RC, although both displayed similar stability in the PC (−58.5 kcal mol^{-1} and −58.9 kcal mol^{-1}, respectively). These findings reveal distinct stabilization patterns in both RC and PC, strongly dependent on the electronic nature of the nucleophile. Notably, the product complexes are more stable in all cases than the reactant complexes, resulting in negative reaction energies (Table 1), both in terms of electronic energy and Gibbs free energy, thereby characterizing the overall process as exothermic and exergonic. This observation aligns with the increased strength of the bond formed after substitution, except for Br^- as a nucleophile, suggesting that in this set of S_N2 reactions, thermodynamic factors may contribute significantly to lowering the activation barrier. Such a driving force could potentially contribute to lowering the activation barrier.

The quantitative analysis of activation barriers shows significant trends that deserve closer examination (see Table 1). In the halogenated nucleophile series, an unusual ascending order was observed: F^- (10.9 kcal mol^{-1}) < Br^- (17.9 kcal mol^{-1}) < Cl^- (20.6 kcal mol^{-1}). This pattern, observed in this specific halide series, does not align with expectations based on periodic trends like nucleophile electronegativity or polarizability. Among oxygen-, nitrogen-, and sulfur-based nucleophiles, both simple and substituted, the following patterns were identified: H_2N^- (5.9 kcal mol^{-1}) < HO^- (6.4 kcal mol^{-1}) < HS^- (14.4 kcal mol^{-1}), and $MeNH^-$ (3.9 kcal mol^{-1}) < MeO^- (7.1 kcal mol^{-1}) < MeS^- (10.8 kcal mol^{-1}). Again, within the nucleophile subsets analyzed here, these trends do not adhere to predictable patterns based solely on periodic properties. In contrast, nucleophiles with α-substituents exhibited divergent behavior relative to their parent

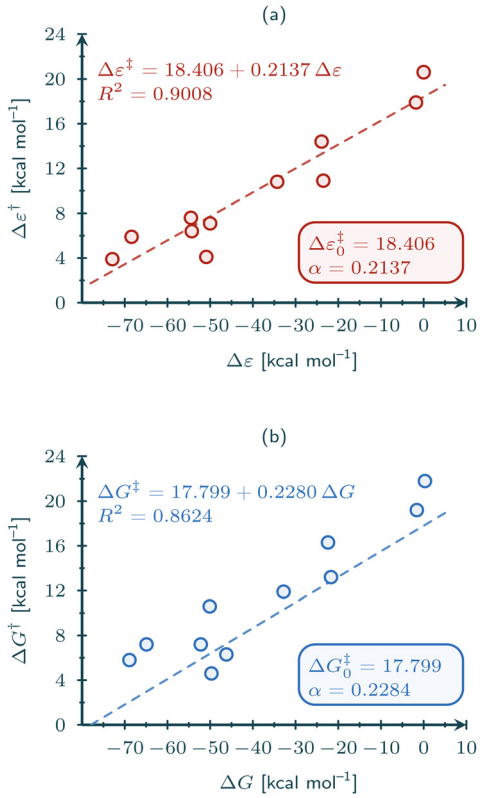

Fig. 3 Activation barrier as function of the reaction energy for the S_N2 reaction of chloromethane with different nucleophiles. Data are shown as (a) electronic energies (ε) and (b) Gibbs free energies (G).

nucleophiles: HOO^- showed a lower barrier (4.1 kcal mol^{-1}) than both the simple and substituted oxygen nucleophiles, whereas $HSHN^-$ exhibited a higher barrier (7.6 kcal mol^{-1}) than its nitrogen-based analogues. This variation suggests that, for the studied systems, the presence of α-substituents can significantly alter the relative reactivity of the nucleophilic center,[85] in line with previous reports on α-substituent effects. Despite the barriers calculated under the continuum approximation coinciding with the experimental trends observed for certain nucleophiles,[86,87] the lack of a systematic correlation in the activation barriers, which remains consistent even after single-point refinement at the CCSD(T) level (Table 1), indicates that, within the present set of nucleophiles, the atomic identity of the nucleophile does not solely determine reactivity but is likely strongly modulated by global thermodynamic factors, as reflected in the reaction energies, calculated both as electronic and Gibbs free energies, which vary significantly across the nucleophile series (see Table 1).

Fig. 3 shows the relationship between the activation barriers and the reaction energies for the series of nucleophiles studied, clearly revealing an approximately linear trend. Within the studied series of nucleophiles, exothermic and exergonic reactions tend to exhibit lower activation barriers, whereas less thermodynamically favorable processes present higher ones; moreover, the degree of exothermicity varies systematically with the electronic nature of the nucleophile. A linear fit based on the model proposed by Laffler yielded the characteristic

parameters for this ($\Delta\varepsilon_0^{\ddagger}$ and $\Delta G_0^{\ddagger}$) and the Brønsted slope (α). These results indicate that, for the analyzed chloromethane-based S_N2 reactions, thermodynamic factors significantly influence the observed reactivity, as evidenced by the strong linear correlation between barriers and reaction energies ($R^2 \approx 0.90$) observed within this specific dataset.

A logical strategy to isolate the effect of the hyperconjugative interaction $n_{Nu} \rightarrow \sigma^*_{C-Cl}$ would involve repeating this analysis while explicitly turning off such donor–acceptor interactions, thereby evaluating their impact on $\Delta\varepsilon_0^{\ddagger}$, $\Delta G_0^{\ddagger}$, and α intrinsic parameters. However, the methodological tools required to selectively deactivate electronic interactions are only functionally available within the HF framework, which lacks the electronic correlation effects essential for accurately describing anionic systems such as those investigated here. To further support this limitation, we estimated activation barriers and reaction energies at the HF level (Table 1), which yielded significantly overestimated values compared to correlated methods. For this reason, we adopted the quadratic Marcus' model, as it offers a more general and physically consistent framework for estimating intrinsic barriers, allowing the measure of reactivity free from thermodynamic bias. This approach ensures that the derived trends reflect intrinsic electronic and structural effects rather than artifacts introduced by insufficient correlation treatment.

3.2 Barrier deconvolution

Eqn (2) (described in the Computational details and models section) was employed to calculate the intrinsic barrier for each of the reaction analyzed. Calculations were performed using both ε and G, and the results are presented in Table 2. In all cases, the intrinsic barriers estimated *via* Marcus' model were consistently greater than the apparent barriers, since the correction term (Δ_{corr}), defined as the intrinsic activation barrier minus the apparent activation barrier, was generally positive.

Table 2 Intrinsic barriers calculated using eqn (2) and corresponding correction terms for the S_N2 reaction of chloromethane with various nucleophiles, using electronic energies (ε) and Gibbs free energies (G). All values are reported in kcal mol^{-1}

Nu	$\Delta_0\varepsilon^{\ddagger}$	Δ_{corr}[a]	$\Delta_0 G^{\ddagger}$	Δ_{corr}[b]
Halide nucleophiles				
F^-	21.0	10.1	22.8	9.6
Cl^-	20.6	0.0	21.7	−0.1
Br^-	18.8	0.9	20.0	0.8
Simple nucleophiles				
H_2N^-	30.5	24.6	31.2	24.0
HO^-	26.6	20.2	27.0	19.8
HS^-	24.9	10.5	26.3	10.0
Substituted nucleophiles				
CH_3HN^-	28.9	25.0	30.6	24.7
CH_3O^-	26.1	19.0	23.8	17.5
CH_3S^-	25.0	14.2	25.7	13.8
Nucleophiles with α-substituents				
HOO^-	22.3	18.2	22.7	18.0
$HSHN^-$	28.2	20.7	30.5	19.9

[a] $\Delta_{corr} = \Delta\varepsilon_0^{\ddagger} - \Delta\varepsilon^{\ddagger}$. [b] $\Delta_{corr} = \Delta G_0^{\ddagger} - \Delta G^{\ddagger}$.

This outcome aligns with the physical interpretation of the model: for the highly exothermic reactions studied, the reaction energy serves as a driving force that reduces the effective barrier height. Deconvolution thus allows one to quantify the minimal energy required to reach the transition state without thermodynamic effects.

The intrinsic barriers obtained revealed coherent trends within the analyzed nucleophile families, emphasizing how their electronic character influences the inherent reactivity in the chloromethane-based S_N2 context. In the halide series, a consistent trend was noted for both electronic energies and Gibbs free energies: Br^- (18.8 kcal mol^{-1} for electronic energy and 20.0 kcal mol^{-1} for Gibbs free energy) < Cl^- (20.6 kcal mol^{-1} and 21.7 kcal mol^{-1}) < F^- (21.0 kcal mol^{-1} and 22.8 kcal mol^{-1}). This behavior contrasts with that observed for the apparent barriers but, across this subset, appears to align with periodic trends such as electronegativity and polarizability, suggesting a consistent electronic contribution. For simple nucleophiles derived from nitrogen, oxygen, and sulfur, a descending trend was identified down the group: H_2N^- (30.5 kcal mol^{-1}) > HO^- (26.6 kcal mol^{-1}) > HS^- (24.9 kcal mol^{-1}) when using electronic energies, and H_2N^- (31.2 kcal mol^{-1}) > HO^- (27.0 kcal mol^{-1}) > HS^- (26.3 kcal mol^{-1}) when using Gibbs free energies. This suggests that periodic properties may influence the magnitude of the intrinsic barrier. A similar trend was observed in the substituted analogues, where the values were 28.9, 26.1, and 25.0 kcal mol^{-1} for $MeNH^-$, MeO^-, and MeS^-, respectively, when considering electronic energy. However, when Gibbs free energies were used, the relative order changed to $MeNH^-$ (30.6 kcal mol^{-1}) > MeS^- (25.7 kcal mol^{-1}) > MeO^- (23.8 kcal mol^{-1}).

Finally, nucleophiles bearing α-substituents preserved the reactivity order previously observed: HOO^- showed intrinsic barriers of 22.3 kcal mol^{-1} (electronic) and 22.7 kcal mol^{-1} (Gibbs), while $HSHN^-$ exhibited higher values of 28.2 and 30.5 kcal mol^{-1}. This difference supports the conclusion that, in the context of the chloromethane-based S_N2 reactions studied, HOO^- is more reactive than $HSHN^-$, both in terms of apparent and intrinsic barriers. Moreover, both nucleophiles displayed lower intrinsic barriers than their simple and substituted analogues, suggesting that, for the considered nucleophiles, the electronic effects associated with α-substituents contribute favorably to the activation process.

Altogether, these findings indicate that, in the present set of S_N2 reactions, thermodynamic corrections not only change the absolute values of activation barriers but can also affect the relative reactivity order among different nucleophiles. The shift in trends observed before and after deconvolution highlights the importance of distinguishing between intrinsic effects and thermodynamic contributions when interpreting activation profiles. Access to intrinsic barriers offers a direct measure of the energy cost associated with reaching the transition state and consistently reflects the electronic nature of the nucleophilic center, representing a valuable step toward understanding the electronic factors that govern reactivity in S_N2 reactions involving nucleophiles with diverse electronic profiles.

3.3 Structural analysis

A geometric analysis of the reactant complex and the transition state was conducted to elucidate the structural features that precede and accompany the nucleophilic substitution event in the modeled reactions. This point of view aims to identify early-stage stabilizing interactions and to evaluate the extent of spatial preorganization involved in the approach of the nucleophile within the reactant complexes studied, leading to the corresponding transition states. A comparative analysis across the studied nucleophiles enables the identification of structural trends that, within this dataset, may anticipate the facility of the S_N2 process and correlate with the magnitude of the intrinsic activation barrier. The geometric parameters considered in this study include the distance between the nucleophile and the electrophilic carbon (d_{Nu-C}), the length of the leaving bond (d_{C-Cl}), the attack angle defined by the Nu–C–Cl atoms (θ), and an improper dihedral angle (ϕ) used as a measure of distortion from the ideal tetrahedral geometry of the central carbon. The latter refers to the angle formed between two planes: one that includes the three hydrogen atoms of the methyl group and the other that includes the carbon atom and two of those three hydrogens. A schematic representation of these parameters and their numerical values are provided in Table 3.

In the analyzed systems, the structural analysis of reactant complexes typically reveals a spatial arrangement consistent with an S_N2 mechanism. In most cases, the Nu–C–Cl angle approaches 180°, which corresponds to the expected colinear orientation for bimolecular nucleophilic substitution. However, in systems with oxygen-based nucleophiles such as HO^-, MeO^-, and HOO^-, a significant deviation from this ideal geometry is observed (the optimized geometries are shown in Fig. S1). For HO^- and MeO^-, the unexpected configuration can be attributed to the formation of a C–H···O hydrogen bond (1.733 Å and 1.818 Å for HO^- and MeO^-, respectively). This interaction is hypothesized based on the optimized geometry adopted by the nucleophile relative to the electrophile in these systems. In the case of HOO^-, although no specific interaction of this kind can be assumed due to its lower basicity and H acceptor capacity, the angular deviation may reflect the presence of an alternative stabilizing effect. In all analyzed cases, the reactant complexes exhibit incipient interaction between the nucleophile and the electrophilic carbon, as evidenced by moderately shortened Nu–C distances (ranging from 2.836 to 3.733 Å) and elongation of the C–Cl bond relative to free chloromethane (see note in Table 3), indicating early polarization of the reactive center. This variability in d_{Nu-C} depends not only on the size of the nucleophile but also on its electronic nature and ability to establish attractive interactions. Introducing a methyl group into O-, S-, and N-based nucleophiles leads to a systematic shortening of the Nu–C distance compared to their unsubstituted analogues, which may suggest enhanced nucleophilic efficiency in the context of the studied systems. Among the systems analyzed, HOO^- exhibits the shortest Nu–C distance and the greatest C–Cl elongation, which may reflect a more favorable structural preactivation in terms of geometry. Finally, analysis of the improper dihedral angle produced values comparable to free chloromethane. This indicates that, in the reactant complexes examined, a significant geometric reorganization toward a pseudoplanar configuration has not yet occurred at this stage.

Upon reaching the transition state, the optimized structures exhibit substantial geometric changes in the above mentioned parameters. The Nu–C distance shortens significantly, with values ranging from 1.956 to 2.424 Å, indicating considerable progress in forming the new bond. Complementarily, the C–Cl distance increases relative to the reactant complex, exceeding 2.001 Å, consistent with the progressive rupture of the leaving bond. These observations are consistent with a concerted process as expected for the S_N2 mechanism in the studied systems. Comparing the bond lengths of Nu–C and C–Cl shows significant asynchronicity in most systems, except for the Cl^- nucleophile. In all the analyzed cases, the Nu–C–Cl angle converges toward values near 180°, reflecting a colinear arrangement in the transition region. Similarly, the improper dihedral angle decreases to values below 20.2°, indicating a transition from tetrahedral geometry to a pseudoplanar configuration. This reduction in tetrahedral character aligns with the expected geometry of the transition state, and the resulting degree of planarity varies depending on the type of nucleophile involved which is consistent with the reaction's exothermicity. As postulated by Hammond's principle, more exothermic reactions tend to exhibit transition states that

Table 3 Characteristic geometric parameters of the reactant complex and transition state optimized at the MP2-SMD(THF)/cc-pVTZ level for the S_N2 reaction of chloromethane with various nucleophiles. Distances are reported in ångströms (Å) and angles in degrees (°)

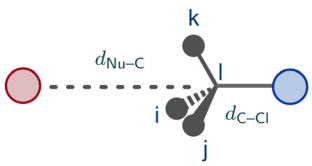

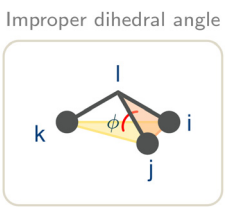

	Reactant complex (RC)				Transition state (TS)			
	d_{Nu-C}	d_{C-Cl}	θ	ϕ	d_{Nu-C}	d_{C-Cl}	θ	ϕ
Halide nucleophiles								
F^-	3.337	1.791	179.9	33.9	1.956	2.138	179.8	7.6
Cl^-	3.569	1.794	179.6	33.5	2.279	2.279	179.9	0.0
Br^-	3.474	1.800	179.8	33.6	2.424	2.272	179.9	1.3
Simple nucleophiles								
H_2N^-	3.376	1.798	177.8	33.5	2.376	2.027	179.9	19.1
HO^-	2.853	1.806	115.5	32.4	2.229	2.010	179.8	20.2
HS^-	3.733	1.794	177.9	33.6	2.474	2.182	179.9	8.1
Substituted nucleophiles								
CH_3HN^-	3.230	1.800	171.2	33.2	2.369	2.001	175.8	20.0
CH_3O^-	2.923	1.800	112.4	32.4	2.150	2.028	179.2	16.8
CH_3S^-	3.512	1.799	168.3	33.4	2.502	2.134	176.3	11.3
Nucleophiles with α-substituents								
HOO^-	2.836	1.812	158.6	33.6	2.157	2.027	176.9	17.7
$HSHN^-$	3.248	1.798	177.4	33.4	2.248	2.063	177.6	15.0

The geometric parameters of isolated chloromethane calculated at the same level of theory are d_{C-Cl} = 1.786 Å and ϕ = 33.5°.

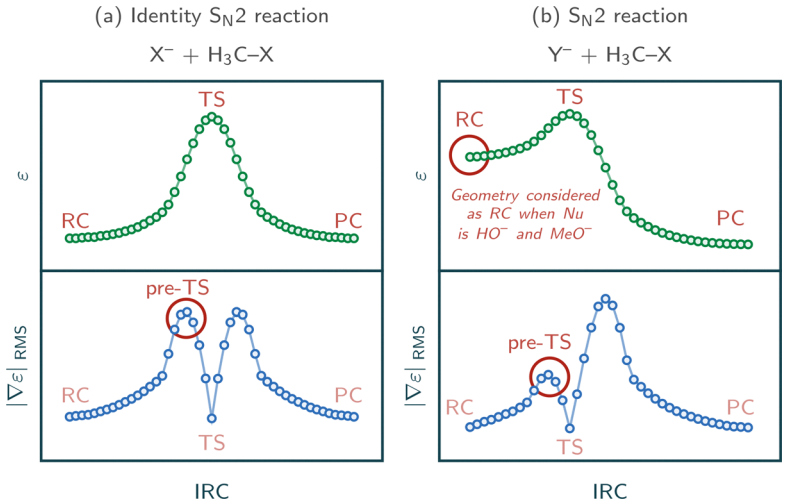

Fig. 4 Representative IRC profiles for (a) identity and (b) asymmetric S_N2 reactions: electronic energy (ε) and Laplacian curvature ($|\nabla\varepsilon|_{RMS}$) highlighting the pre-TS point.

resemble the reactants more closely.[88] This trend is observed in the analyzed systems, where increased exothermicity correlates with a lower degree of planarity in the S_N2 transition state.

Comparing the structural parameters of the reactant complex and the transition state, in these systems, illustrates the molecular rearrangement associated with the S_N2 mechanism. The lack of significant distortion at the electrophilic center in the reactant complex, as indicated by the improper dihedral angle values, suggests that structural reorganization primarily begins when approaching the transition state. Nevertheless,

Table 4 NBOs[ab] (isosurface = 0.1 a.u.) and topological characterization of Nu–C interactions for halide nucleophiles: $E^{(2)}_{n\to\sigma^*}$ stabilization energies and QTAIM descriptors (ρ_{BCP} and $|V_{BCP}|/G_{BCP}$) at the Nu–C bond critical point

Nu	RC		pre-TS	
F^-	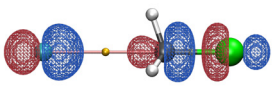		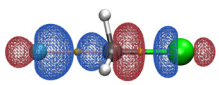	
	$n_F \to \sigma^*_{C-Cl}$	0.78 kcal mol^{-1}	$n_F \to \sigma^*_{C-Cl}$	28.69 kcal mol^{-1}
	ρ_{BCP}	0.0043 a.u.	ρ_{BCP}	0.0409 a.u.
	$\lvert V_{BCP}\rvert/G_{BCP}$	0.7460	$\lvert V_{BCP}\rvert/G_{BCP}$	0.9846
Cl^-	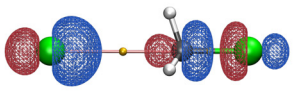		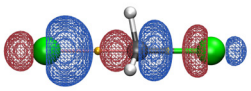	
	$n_{Cl} \to \sigma^*_{C-Cl}$	1.29 kcal mol^{-1}	$n_{Cl} \to \sigma^*_{C-Cl}$	33.56 kcal mol^{-1}
	ρ_{BCP}	0.0049 a.u.	ρ_{BCP}	0.0343 a.u.
	$\lvert V_{BCP}\rvert/G_{BCP}$	0.7053	$\lvert V_{BCP}\rvert/G_{BCP}$	1.0788
Br^-	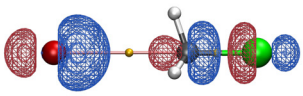		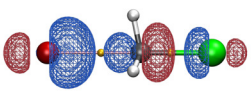	
	$n_{Br} \to \sigma^*_{C-Cl}$	2.52 kcal mol^{-1}	$n_{Br} \to \sigma^*_{C-Cl}$	37.53 kcal mol^{-1}
	ρ_{BCP}	0.0069 a.u.	ρ_{BCP}	0.0320 a.u.
	$\lvert V_{BCP}\rvert/G_{BCP}$	0.7572	$\lvert V_{BCP}\rvert/G_{BCP}$	1.0986

[a] In some cases, NBO analysis identified two $n_{Nu} \to \sigma^*_{C-Cl}$ interactions, associated with lone pairs of different orbital characters (s and p). Reported values correspond to the sum of both contributions; the visualized orbital is the one with greater p-character. This criterion was applied consistently to the entire nucleophile series. [b] In some orbital visualizations, donor and acceptor lobes may appear with the opposite phase; however, as discussed in the Computational details and models section, this does not affect the interaction.

initial changes in parameters such as the Nu–C distance and the attack angle point to the presence of early interactions, which may help facilitate reaching the transition state. In this context, characterizing the electronic nature of these interactions may provide valuable insight into the origin of the trends previously observed in the intrinsic barriers within this set of S_N2 reactions.

3.4 Understanding intrinsic reactivity

This section aims to clarify the differences observed in the intrinsic barriers and structural parameters discussed earlier by focusing on the electronic characteristics of key intermediates in the modeled S_N2 reactions. We will use two complementary theoretical frameworks: NBO analysis and QTAIM. Representative geometries were selected for electronic analysis to capture the relevant interactions during the reaction: the RC, which reveals early-stage interactions, and the TS, where these interactions reach their maximum intensity. In some oxygen nucleophiles such as HO^- and MeO^-, the RC does not exhibit the ideal alignment between the nucleophile and the electrophile, a requirement for the proper electronic characterization; for these cases, the reactant-side endpoint of the intrinsic reaction coordinate (IRC) was used as a substitute (see Fig. 4). Additionally, in some systems with nearly zero improper dihedral angles, reliable NBO analysis could not be performed on the TS due to the loss of orbital identity between fragments. As an alternative to circumvent the cited inconveniences, a pre-TS geometry, defined as the structure corresponding to the maximum RMS gradient norm ($|\nabla\varepsilon|_{RMS}$) preceding the transition state, was systematically employed throughout this study to ensure methodological consistency across the considered nucleophile series. This structure preserves orbital partitioning between fragments and appropriately represents the pre-transition region. Comparisons between nucleophiles were restricted to members of the same family or period of the periodic table to ensure consistency based on established periodic trends. Tables 4–7 present the electronic characterization of the aforementioned complexes. These results include graphical visualizations of NBOs and BCPs, along with their respective bond paths. Furthermore, the tables provide the $E^{(2)}_{n\to\sigma^*}$ stabilization energies associated with hyperconjugative interactions, as well as topological properties such as ρ_{BCP} and $|V_{BCP}|/G_{BCP}$.

3.4.1 Halide nucleophiles (Table 4). The combined NBO–QTAIM analysis for this series reveals the presence of an early hyperconjugative interaction of the type $n_{Nu} \rightarrow \sigma^*_{C-Cl}$ in the RC, accompanied by a bond path linking the nucleophile and the electrophilic carbon. The $E^{(2)}_{n\to\sigma^*}$ stabilization energy increases along the series F^- (0.78 kcal mol^{-1}) < Cl^- (1.29 kcal mol^{-1}) < Br^- (2.52 kcal mol^{-1}), in line with the increasing polarizability of the nucleophile and the observed elongation of the C–Cl bond. This trend persists in the pre-transition configuration, with $E^{(2)}_{n\to\sigma^*}$ values reaching 28.69, 33.56, and 37.53 kcal mol^{-1}, respectively. In the halide nucleophile series, natural orbital

Table 5 NBOs (isosurface = 0.1 a.u.) and topological characterization of Nu–C interactions for simple nucleophiles derived from N, O, and S: $E^{(2)}_{n\to\sigma^*}$ stabilization energies and QTAIM descriptors (ρ_{BCP} and $|V_{BCP}|/G_{BCP}$) at the Nu–C bond critical point

Nu	RC		pre-TS	
H_2N^-	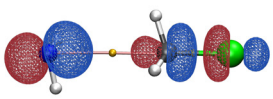		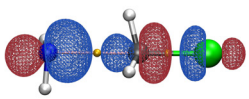	
	$n_{H_2N^-} \rightarrow \sigma^*_{C-Cl}$	1.82 kcal mol^{-1}	$n_{H_2N^-} \rightarrow \sigma^*_{C-Cl}$	21.50 kcal mol^{-1}
	ρ_{BCP}	0.0069 a.u.	ρ_{BCP}	0.0285 a.u.
	$\lvert V_{BCP}\rvert/G_{BCP}$	0.8341	$\lvert V_{BCP}\rvert/G_{BCP}$	1.0110
HO^-	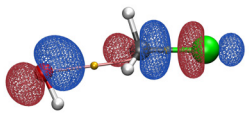		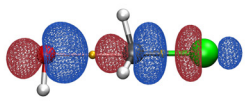	
	$n_{HO^-} \rightarrow \sigma^*_{C-Cl}$	5.80 kcal mol^{-1}	$n_{HO^-} \rightarrow \sigma^*_{C-Cl}$	21.74 kcal mol^{-1}
	ρ_{BCP}	0.0164 a.u.	ρ_{BCP}	0.0322 a.u.
	$\lvert V_{BCP}\rvert/G_{BCP}$	0.8941	$\lvert V_{BCP}\rvert/G_{BCP}$	0.9852
HS^-	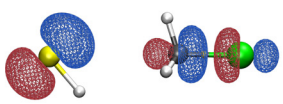		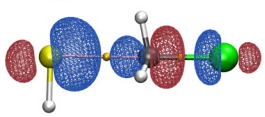	
	$n_{HS^-} \rightarrow \sigma^*_{C-Cl}$	0.86 kcal mol^{-1}	$n_{HS^-} \rightarrow \sigma^*_{C-Cl}$	33.83 kcal mol^{-1}
	ρ_{BCP}	n.d. [a]	ρ_{BCP}	0.0298
	$\lvert V_{BCP}\rvert/G_{BCP}$	n.d. [a]	$\lvert V_{BCP}\rvert/G_{BCP}$	1.0938

[a] Not determined (n.d.) due to the absence of BCP(S–C) in the QTAIM analysis.

visualization shows a collinear alignment between the donor orbital and the C–Cl bond axis, favoring efficient overlap with the σ^*_{C-Cl} orbital. Simultaneously, both ρ_{BCP} and the $|V_{BCP}|/G_{BCP}$ ratio increase from the RC to the pre-TS geometry, indicating a progressive strengthening of the Nu–C interaction. In the pre-TS, ρ_{BCP} decreases in the order $F^- > Cl^- > Br^-$, consistent with greater electron concentration in more electronegative and compact nucleophiles, while $|V_{BCP}|/G_{BCP}$ increases, better capturing the role of polarizability. This dual topological-orbital correlation aligns with the observed trend in intrinsic barriers (21.0, 20.6, and 18.8 kcal mol^{-1}), suggesting that, within this subset, both descriptors consistently track the evolution of interaction strength, in agreement with the intrinsic reactivity trends.

3.4.2 Simple nucleophiles (Table 5). For the series of simple nucleophiles derived from nitrogen, oxygen, and sulfur, the $n_{Nu} \rightarrow \sigma^*_{C-Cl}$ hyperconjugative interaction is observed in the RC of each system. $E^{(2)}_{n\rightarrow\sigma^*}$ increases in the order HS^- (0.86 kcal mol^{-1}) < H_2N^- (1.82 kcal mol^{-1}) < HO^- (5.80 kcal mol^{-1}), consistent with the relative stabilities derived from electronic energies (Table S1). However, within this series, the trend does not align with the expected polarizability of the nucleophilic centers, particularly in the case of HS^-. Here, the weak interaction appears to arise from an unfavorable alignment of the donor orbital, as suggested by orbital visualizations. As the system progresses toward the pre-transition geometry, $E^{(2)}_{n\rightarrow\sigma^*}$ increases significantly, reaching 21.50, 21.74, and 33.83 kcal mol^{-1} for H_2N^-, HO^-, and HS^-, respectively. This rise is consistent with the decreasing trend in intrinsic barriers calculated using electronic energy for the same nucleophiles (30.5, 26.6, and 24.9 kcal mol^{-1}; see Table 3). Topological analysis for these nucleophiles further supports this interpretation: in the pre-TS region, ρ_{BCP} decreases following the electronegativity of the nucleophiles, while the $|V_{BCP}|/G_{BCP}$ ratio increases in accordance with their polarizability. This dual behavior is particularly evident when comparing the H_2N^-:HO^- and HO^-:HS^- pairs.

3.4.3 Substituted nucleophiles (Table 6). The substituted nucleophiles $MeHN^-$, MeO^-, and MeS^- exhibit behavior similar to their simple analogues H_2N^-, HO^-, and HS^-, both in the evolution of the donor–acceptor interaction and the associated topological descriptors. In the geometry of the RC, $E^{(2)}_{n\rightarrow\sigma^*}$ increases in the order $MeHN^-$ (1.85 kcal mol^{-1}) < MeS^- (1.95 kcal mol^{-1}) < MeO^- (5.04 kcal mol^{-1}), which appears to be driven by the high electron density localized on the oxygen atom and a geometry that favors donor–acceptor overlap

Table 6 NBOs (isosurface = 0.1 a.u.) and topological characterization of Nu–C interactions for substituted nucleophiles derived from N, O, and S: $E^{(2)}_{n\rightarrow\sigma^*}$ stabilization energies and QTAIM descriptors (ρ_{BCP} and $|V_{BCP}|/G_{BCP}$) at the Nu–C bond critical point

Nu	RC		pre-TS	
$MeHN^-$	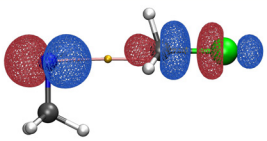		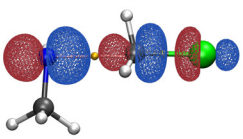	
	$n_{MeHN^-} \rightarrow \sigma^*_{C-Cl}$	1.85 kcal mol^{-1}	$n_{MeHN^-} \rightarrow \sigma^*_{C-Cl}$	19.61 kcal mol^{-1}
	ρ_{BCP}	0.0086 a.u.	ρ_{BCP}	0.0300 a.u.
	$\lvert V_{BCP}\rvert/G_{BCP}$	0.8412	$\lvert V_{BCP}\rvert/G_{BCP}$	1.0348
MeO^-	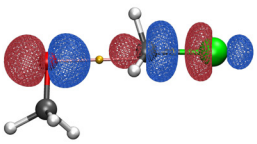		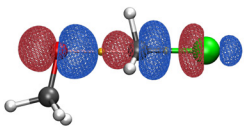	
	$n_{MeO^-} \rightarrow \sigma^*_{C-Cl}$	5.04 kcal mol^{-1}	$n_{MeO^-} \rightarrow \sigma^*_{C-Cl}$	24.37 kcal mol^{-1}
	ρ_{BCP}	0.0166 a.u.	ρ_{BCP}	0.0383 a.u.
	$\lvert V_{BCP}\rvert/G_{BCP}$	0.8880	$\lvert V_{BCP}\rvert/G_{BCP}$	1.0260
MeS^-	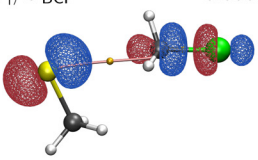		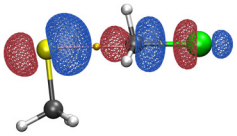	
	$n_{MeS^-} \rightarrow \sigma^*_{C-Cl}$	1.95 kcal mol^{-1}	$n_{MeS^-} \rightarrow \sigma^*_{C-Cl}$	29.30 kcal mol^{-1}
	ρ_{BCP}	0.0070	ρ_{BCP}	0.0298
	$\lvert V_{BCP}\rvert/G_{BCP}$	0.7848	$\lvert V_{BCP}\rvert/G_{BCP}$	1.0938

in MeO. This trend is supported by the ρ_{BCP} values (0.0086, 0.0070, and 0.0166 a.u. for $MeHN^-$, MeS^-, and MeO^-, respectively) and partially reflected in the $|V_{BCP}|/G_{BCP}$ ratio, ranging from 0.7848 (MeS^-) to 0.8880 (MeO^-). Upon reaching the pre-TS geometry, all systems exhibit a significant increase in $E^{(2)}_{n\to\sigma^*}$, with values of 19.61, 24.37, and 29.30 kcal mol^{-1} in the order $MeHN^- < MeO^- < MeS^-$. In this subset, this progression correlates with enhanced donor orbital coupling, increasingly favored by the nucleophile's polarizability. In this same geometry, ρ_{BCP} and $|V_{BCP}|/G_{BCP}$ reach maxima in MeO^- and MeS^-, respectively, reflecting, in these systems, the interplay between the charge concentration (electronegativity) and diffuseness (polarizability) of the nucleophilic center. Finally, the intrinsic activation barriers computed using electronic energies follow the trend $MeHN^-$ (28.9 kcal mol^{-1}) > MeO^- (26.1 kcal mol^{-1}) > MeS^- (25.0 kcal mol^{-1}), consistent with the periodic properties of each nucleophile's heteroatom, as reflected in the electronic descriptors analyzed.

3.4.4 Nucleophiles with α-substituents (Table 7). For the α-substituted nucleophiles studied ($HSHN^-$ and HOO^-), the electronic analysis reveals distinct characteristics compared to their non-substituted counterparts. In the reactant complex, the main $n_{Nu} \to \sigma^*_{C-Cl}$ interaction displays $E^{(2)}_{n\to\sigma^*}$ values of 1.44 and 3.72 kcal mol^{-1} for $HSHN^-$ and HOO^-, respectively. Only $HSHN^-$ shows a bond path between the nucleophilic nitrogen and the electrophilic carbon, whereas HOO^- lacks this connection but exhibits a secondary C–H···O hydrogen bond interaction between the α-oxygen and a methyl hydrogen from the electrophile, pointing to early-stage non-covalent stabilization, as evidenced by a well-defined bond path and a substantial $E^{(2)}_{n\to\sigma^*}$ interaction indicative of electron delocalization (for this weak interaction, $E^{(2)}_{n\to\sigma^*}$ = 4.89 kcal mol^{-1}, ρ_{BCP} = 0.0214 a.u., and $|V_{BCP}|/G_{BCP}$ = 0.8823). In the pre-transition region, $E^{(2)}_{n\to\sigma^*}$ increases to 21.95 ($HSHN^-$) and 23.79 kcal mol^{-1} (HOO^-), accompanied by increased ρ_{BCP} (0.0327 and 0.0378 a.u.) and higher $|V_{BCP}|/G_{BCP}$ values (1.0393 and 1.0229), consistent with stronger attractive interactions in the transition region of the modeled systems. Despite comparable $E^{(2)}_{n\to\sigma^*}$ between the α-substituted nucleophile and simple and substituted analogues, the former's intrinsic barriers are significantly lower, 22.3 kcal mol^{-1} for HOO^- and 28.2 for $HSHN^-$, suggesting that, in these cases, beyond the primary donor–acceptor interaction, additional electronic contributions involving the α-substituent and the electrophile may effectively stabilize the system in the transition region, thereby lowering the intrinsic activation barrier. This observation aligns with previous reports in other organic systems, where non-covalent contributions, particularly through interactions between the nucleophile and C–H bonds of the electrophile, have been shown to influence the activation process.[89]

In summary, the combined NBO-QTAIM analysis for the studied systems reveals the presence of early donor–acceptor interactions in the reactant complexes, which become significantly stronger near the transition state geometry. Fig. 5 illustrates the intrinsic activation barriers alongside the hyperconjugative stabilization energies computed at the pre-transition state geometries. Within the studied reaction set, an inverse trend is observed: systems exhibiting higher activation barriers (red and blue bars) tend to show lower $E^{(2)}_{n\to\sigma^*}$ values (green bars), whereas lower barriers are consistently associated with stronger hyperconjugative interactions. This relationship highlights, in the context of the modeled S_N2

Table 7 NBOs (isosurface = 0.1 a.u.) and topological characterization of Nu–C interactions for substituted nucleophiles with α-substituents: $E^{(2)}_{n\to\sigma^*}$ stabilization energies and QTAIM descriptors (ρ_{BCP} and $|V_{BCP}|/G_{BCP}$) at the Nu–C bond critical point

Nu	RC		pre-TS	
$HSHN^-$	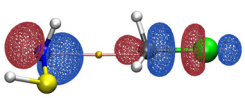		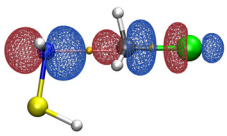	
	$n_{HSHN^-} \to \sigma^*_{C-Cl}$	1.44 kcal mol^{-1}	$n_{HSHN^-} \to \sigma^*_{C-Cl}$	21.95 kcal mol^{-1}
	ρ_{BCP}	0.0076 a.u.	ρ_{BCP}	0.0327 a.u.
	$\lvert V_{BCP}\rvert/G_{BCP}$	0.8071	$\lvert V_{BCP}\rvert/G_{BCP}$	1.0393
HOO^-	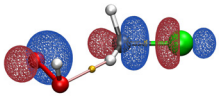		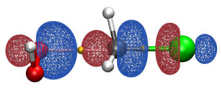	
	$n_{HOO^-} \to \sigma^*_{C-Cl}$	3.72 kcal mol^{-1}	$n_{HOO^-} \to \sigma^*_{C-Cl}$	23.79 kcal mol^{-1}
	ρ_{BCP}	n.d. [a]	ρ_{BCP}	0.0378
	$\lvert V_{BCP}\rvert/G_{BCP}$	n.d. [a]	$\lvert V_{BCP}\rvert/G_{BCP}$	1.0229

[a] Not determined (n.d.) due to the absence of BCP(O–C) in the QTAIM analysis.

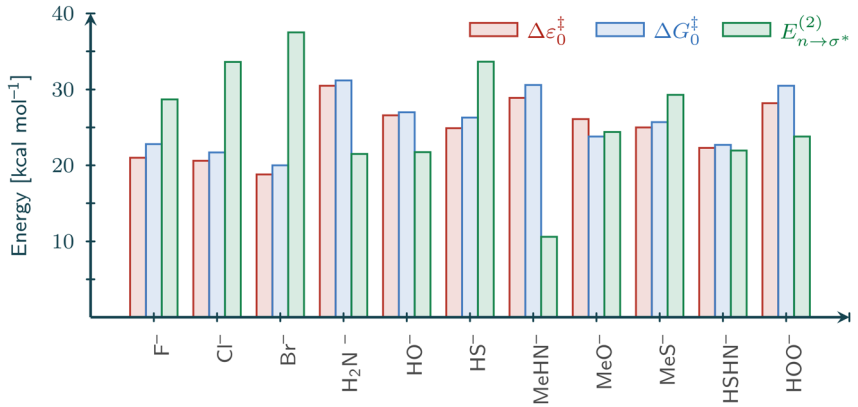

Fig. 5 Electronic ($\Delta\varepsilon_0^{\ddagger}$) and Gibbs free ($\Delta G_0^{\ddagger}$) intrinsic barriers and second-order hyperconjugative stabilization energies ($E^{(2)}_{n\to\sigma^*}$) for each nucleophile, computed at the MP2-SMD(THF)/cc-pVTZ level.

reactions, the important role of the nucleophile's capacity to modulate the interaction strength with the electrophilic center, thereby compensating for the energetic demands of the structural reorganization occurring at the transition state. In this study, the topological parameters ρ_{BCP} and $|V_{BCP}|/G_{BCP}$ further support these findings by providing a complementary perspective on the nature of bonding: ρ_{BCP} reflects local electron density concentration, while the $|V_{BCP}|/G_{BCP}$ ratio indicates the degree of electron sharing, highlighting how both electronegativity and polarizability shape the interaction profile.

4 Conclusions

This study aimed to identify the structural and electronic factors that shape intrinsic reactivity in model bimolecular nucleophilic substitution (S_N2) reactions of the type Y + CH_3–Cl, with a particular focus on the $n_{Nu} \rightarrow \sigma^*_{C-Cl}$ hyperconjugation as a stabilizing interaction in the transition region. To this end, quantum chemical calculations were carried out at the MP2-SMD(THF)/cc-pVTZ level of theory, followed by a comprehensive analysis of activation and reaction energies, as well as the geometrical and electronic properties of key intermediates. Crucially, Marcus' theory was applied to deconvolute the apparent activation barriers, allowing us to recover the intrinsic activation component, $\Delta E_0^{\ddagger}$, which is free from thermodynamic bias and reflects the minimal energy requirements for accessing the transition state. NBO and QTAIM analyses were employed to understand the correlation between the reactivity trends and the electronic properties of the nucleophiles investigated in this study.

In the present set of modeled S_N2 reactions, thermodynamic factors appear to play a dominant role in determining the apparent activation barriers. This is supported by the strong correlation observed between barriers and reaction energies, a relationship evident in both electronic and Gibbs free energies. Within this dataset, the strength of the $n_{Nu} \rightarrow \sigma^*_{C-Cl}$ hyperconjugative interaction, represented by $E^{(2)}_{n\to\sigma^*}$, does not correlate with the stability of the reactant complex, suggesting a limited contribution to its thermodynamic stabilization. This may be attributed to the fact that the overall stabilization energy, reflected in electronic and Gibbs free energies, is greater in magnitude than the hyperconjugative contribution alone, implying that other factors govern the complex's stability. Instead, the aforementioned interaction consistently correlates with the intrinsic barriers derived from Marcus' theory. This finding suggests that, in the studied systems, hyperconjugation fundamentally affects intrinsic reactivity by damping the energetic requirements needed to reach the transition state. Furthermore, the observed geometric and energetic trends across different nucleophile families appear to align with periodic properties, such as electronegativity and polarizability, as effectively illustrated by NBO and QTAIM analyses. The examination of reactive complexes and pre-transition states reveals that early donor–acceptor interactions reach their maximum as the system approaches the transition state. The above observation reinforces the idea that, in these reactions, intrinsic electronic organization, rather than mere thermodynamic stabilization, contributes to the barrier height and, consequently, the resulting reactivity trends.

To the best of our knowledge, no systematic analysis has previously quantified the impact of specific electronic interactions, such as $n_{Nu} \rightarrow \sigma^*_{C-Cl}$ hyperconjugation, on the intrinsic activation barrier in non-identity S_N2 reactions. The results presented here suggest that, rather than merely providing passive stabilization, such interactions can serve as crucial electronic elements that fine-tune reactivity in these systems. Overall, our findings enhance the fundamental understanding of the factors influencing nucleophilic efficiency and highlighting the potential of hyperconjugation as an additional structural degree of freedom that could be utilized to modulate substrate reactivity and in predicting trends in regioselectivity. This approach opens new ways for developing more efficient and controllable synthetic strategies in organic chemistry.

Conflicts of interest

There are no conflicts to declare.

Data availability

The data supporting this article have been included as part of the supplementary information (SI). Supplementary information is available. See DOI: https://doi.org/10.1039/d5cp02545a.

Acknowledgements

The authors acknowledge the financial support provided by Dirección General de Asuntos del Personal Académico (DGAPA-IN222924) and the facilities provided by the Dirección General de Cómputo y de Tecnologías de Información y Comunicación (DGTIC-252) at the Universidad Nacional Autónoma de México and the Laboratorio de Supercómputo y Visualización en Paralelo at the Universidad Autónoma Metropolitana. Eduardo H. Huerta (CVU 592116) and Jorge Gutiérrez-Flores (CVU 621254) acknowledge SECIHTI for the postdoctoral fellowship. Marcos Hernández-Rodríguez acknowledge SECIHTI's CF-2023-I-1087 grant.

References

1 I. V. Alabugin, K. M. Gilmore and P. W. Peterson, *Wiley Interdiscip. Rev.: Comput. Mol. Sci.*, 2011, **1**, 109–141.
2 F. Weinhold and C. R. Landis, *The Anomeric Effect and Related Stereoelectronic Effects at Oxygen*, Cambridge University Press, 2005.
3 F. Weinhold, *J. Comput. Chem.*, 2012, **33**, 2363–2379.
4 V. Pophristic and L. Goodman, *Nature*, 2001, **411**, 565–568.
5 F. Weinhold, *Angew. Chem., Int. Ed.*, 2003, **42**, 4188–4194.
6 Y. Mo, W. Wu, L. Song, M. Lin, Q. Zhang and J. Gao, *Angew. Chem., Int. Ed.*, 2004, **43**, 1986–1990.
7 A. J. Kirby, *The Anomeric Effect and Related Stereoelectronic Effects at Oxygen*, Springer Berlin, Heidelberg, 1983.
8 E. Juaristi and G. Cuevas, *Tetrahedron*, 1992, **48**, 5019–5087.
9 I. V. Alabugin, L. Kuhn, N. V. Krivoshchapov, P. Mehaffya and M. G. Medvedev, *Chem. Soc. Rev.*, 2021, **50**, 10212–10252.
10 U. Salzner and P. V. R. Schleyer, *J. Org. Chem.*, 1994, **59**, 2138–2155.
11 G. A. Kasaei, D. Nori-Shargh, H. Yahyaei, S. N. Mousavi and E. Pourdavoodi, *Mol. Simul.*, 2012, **38**, 1022–1031.
12 F. M. Bickelhaupt and E. J. Baerends, *Angew. Chem.*, 2003, **115**, 4315–4320.
13 Y. Mo, *Nat. Chem.*, 2010, **2**, 666–671.
14 B. Gold, G. B. Dudley and I. V. Alabugin, *J. Am. Chem. Soc.*, 2013, **135**, 1558–1569.
15 A. Patel, J. R. Vella, Z.-X. Ma, R. P. Hsung and K. N. Houk, *J. Org. Chem.*, 2015, **80**, 11888–11894.
16 N. Mandal, A. K. Pal, P. Gain, A. Zohaib and A. Datta, *J. Am. Chem. Soc.*, 2020, **142**, 5331–5337.
17 M. Evans and M. Polanyi, *Trans. Faraday Soc.*, 1936, **32**, 1333–1360.
18 R. P. Bell, *Proc. R. Ir. Acad., Sect. A*, 1936, **154**, 414–429.
19 M. G. Evans and M. Polanyi, *Trans. Faraday Soc.*, 1938, **34**, 11–24.
20 J. E. Leffler, *Science*, 1953, **117**, 340–341.
21 R. A. Marcus, *J. Chem. Phys.*, 1965, **43**, 679–701.
22 S. Hoz, H. Basch, J. L. Wolk, T. Hoz and E. Rozental, *J. Am. Chem. Soc.*, 1999, **121**, 7724–7725.
23 I. V. Alabugin, M. Manoharan, B. Breiner and F. D. Lewis, *J. Am. Chem. Soc.*, 2003, **125**, 9329–9342.
24 J. P. Richard and K. B. Williams, *J. Am. Chem. Soc.*, 2007, **129**, 6952–6961.
25 J. Gagnepain, F. Castet and S. Quideau, *Angew. Chem., Int. Ed.*, 2007, **46**, 1533–1535.
26 K. Gilmore, M. Manoharan, J. I.-C. Wu, P. V. R. Schleyer and I. V. Alabugin, *J. Am. Chem. Soc.*, 2012, **134**, 10584–10594.
27 B. Gold, G. B. Dudley and I. V. Alabugin, *J. Am. Chem. Soc.*, 2013, **135**, 1558–1569.
28 A. Patel, J. R. Vella, Z.-X. Ma, R. P. Hsung and K. N. Houk, *J. Org. Chem.*, 2015, **80**, 11888–11894.
29 N. Mandal, A. K. Pal, P. Gain, A. Zohaib and A. Datta, *J. Am. Chem. Soc.*, 2020, **142**, 5331–5337.
30 M. Gallegos, A. Costales and N. Martín Pendás, *J. Comput. Chem.*, 2022, **43**, 785–795.
31 I. Iribarren, C. Trujillo, G. Sánchez-Sanz, E. Hénon, J. Elguero and I. Alkorta, *Theor. Chem. Acc.*, 2023, **142**, 81.
32 T. Hansen, P. Vermeeren, K. W. J. Zijderveld, F. M. Bickelhaupt and T. A. Hamlin, *Chem. – Eur. J.*, 2023, **29**, e202301308.
33 L. R. Domingo, P. Pérez, M. Ríos-Gutiérrez and M. J. Aurell, *Org. Biomol. Chem.*, 2024, **22**, 7425–7437.
34 W. A. Remmerswaal, T. De Jong, K. N. A. Van De Vrande, R. Louwersheimer, T. Verwaal, D. V. Filippov, J. D. C. Codée and T. Hansen, *Chem. – Eur. J.*, 2024, **30**, e202400590.
35 Y. Zhu, Y. Li and D. Wang, *J. Phys. Chem. A*, 2024, **128**, 10766–10774.
36 Y. Orito, *ACS Omega*, 2025, **10**, 9266–9274.
37 G. Vayner, K. N. Houk, W. L. Jorgensen and J. I. Brauman, *J. Am. Chem. Soc.*, 2004, **126**, 9054–9058.
38 S. Liu, H. Hu and L. G. Pedersen, *J. Phys. Chem. A*, 2010, **114**, 5913–5918.
39 T. A. Hamlin, D. M. Swart and F. M. Bickelhaupt, *ChemPhysChem*, 2018, **19**, 1315–1330.
40 J. M. Gonzales, W. D. Allen and H. F. Schaefer, *J. Phys. Chem. A*, 2005, **109**, 10613–10628.
41 M. Breugst, H. Zipse, P. Guthrie and H. Mayr, *Angew. Chem., Int. Ed.*, 2010, **49**, 5165–5169.
42 I. Alkorta, J. C. R. Thacker and P. L. A. Popelier, *J. Comput. Chem.*, 2018, **39**, 546–556.
43 M. J. Frisch, G. W. Trucks, H. B. Schlegel, G. E. Scuseria, M. A. Robb, J. R. Cheeseman, G. Scalmani, V. Barone, G. A. Petersson, H. Nakatsuji, X. Li, M. Caricato, A. V. Marenich, J. Bloino, B. G. Janesko, R. Gomperts, B. Mennucci, H. P. Hratchian, J. V. Ortiz, A. F. Izmaylov, J. L. Sonnenberg, D. Williams-Young, F. Ding, F. Lipparini, F. Egidi, J. Goings, B. Peng, A. Petrone, T. Henderson, D. Ranasinghe, V. G. Zakrzewski, J. Gao, N. Rega, G. Zheng, W. Liang, M. Hada, M. Ehara, K. Toyota, R. Fukuda, J. Hasegawa, M. Ishida, T. Nakajima, Y. Honda, O. Kitao, H. Nakai, T. Vreven, K. Throssell, J. A. Montgomery, Jr., J. E. Peralta, F. Ogliaro, M. J. Bearpark, J. J. Heyd, E. N. Brothers, K. N. Kudin, V. N. Staroverov,

T. A. Keith, R. Kobayashi, J. Normand, K. Raghavachari, A. P. Rendell, J. C. Burant, S. S. Iyengar, J. Tomasi, M. Cossi, J. M. Millam, M. Klene, C. Adamo, R. Cammi, J. W. Ochterski, R. L. Martin, K. Morokuma, O. Farkas, J. B. Foresman and D. J. Fox, *Gaussian~16 Revision C.01*, Gaussian Inc., Wallingford CT, 2016.
44 C. Møller and M. S. Plesset, *Phys. Rev.*, 1934, **46**, 618–622.
45 M. J. Frisch, M. Head-Gordon and J. A. Pople, *Chem. Phys. Lett.*, 1990, **166**, 275–280.
46 M. J. Frisch, M. Head-Gordon and J. A. Pople, *Chem. Phys. Lett.*, 1990, **166**, 281–289.
47 M. Head-Gordon, J. A. Pople and M. J. Frisch, *Chem. Phys. Lett.*, 1988, **153**, 503–506.
48 S. Sæbø and J. Almlöf, *Chem. Phys. Lett.*, 1989, **154**, 83–89.
49 M. Head-Gordon and T. Head-Gordon, *Chem. Phys. Lett.*, 1994, **220**, 122–128.
50 T. H. Dunning, *J. Chem. Phys.*, 1989, **90**, 1007–1023.
51 D. E. Woon and T. H. Dunning, *J. Chem. Phys.*, 1993, **98**, 1358–1371.
52 A. K. Wilson, D. E. Woon, K. A. Peterson and T. H. Dunning, *J. Chem. Phys.*, 1999, **110**, 7667–7676.
53 A. V. Marenich, C. J. Cramer and D. G. Truhlar, *J. Phys. Chem. B*, 2009, **113**, 6378–6396.
54 J. Tomasi, B. Mennucci and R. Cammi, *Chem. Rev.*, 2005, **105**, 2999–3094.
55 W. N. Olmstead and J. I. Brauman, *J. Am. Chem. Soc.*, 1977, **99**, 4219–4228.
56 J. Chandrasekhar, S. F. Smith and W. L. Jorgensen, *J. Am. Chem. Soc.*, 1984, **106**, 3049–3050.
57 A. J. Parker, *Chem. Rev.*, 1969, **69**, 1–32.
58 D. K. Bohme and G. I. Mackay, *J. Am. Chem. Soc.*, 1981, **103**, 978–979.
59 C. Denekamp and Y. Sandlers, *Angew. Chem., Int. Ed.*, 2006, **45**, 2093–2096.
60 W. Tang, J. Zhao, P. Jiang, X. Xu, S. Zhao and Z. Tong, *J. Phys. Chem. B*, 2020, **124**, 3114–3122.
61 R. A. Marcus, *Annu. Rev. Phys. Chem.*, 1964, **15**, 155–196.
62 R. A. Marcus, *J. Am. Chem. Soc.*, 1969, **91**, 7224–7225.
63 R. A. Marcus, *J. Phys. Chem.*, 1968, **72**, 891–899.
64 R. A. Marcus, *Angew. Chem., Int. Ed. Engl.*, 1993, **32**, 1111–1121.
65 R. A. Marcus, *Pure Appl. Chem.*, 1997, **69**, 13–30.
66 S. Gutiérrez-Oliva, B. Herrera and A. Toro-Labbé, *J. Mol. Model.*, 2018, **24**, 104.
67 A. E. Reed and F. Weinhold, *J. Chem. Phys.*, 1983, **78**, 4066–4073.
68 A. E. Reed, R. B. Weinstock and F. Weinhold, *J. Chem. Phys.*, 1985, **83**, 735–746.
69 A. E. Reed and F. Weinhold, *J. Chem. Phys.*, 1985, **83**, 1736–1740.
70 J. Carpenter, PhD thesis, University of Madison, Madison, Madison, 1987.
71 J. Carpenter and F. Weinhold, *J. Mol. Struct.: THEOCHEM*, 1988, **169**, 41–62.
72 A. E. Reed, L. A. Curtiss and F. Weinhold, *Chem. Rev.*, 1988, **88**, 899–926.
73 F. Weinhold and J. Carpenter, *The Structure of Small Molecules and Ions*, Springer US, Boston, MA, 1988.
74 J. A. Bohmann, F. Weinhold and T. C. Farrar, *J. Chem. Phys.*, 1997, **107**, 1173–1184.
75 E. D. Glendening, C. R. Landis and F. Weinhold, *Wiley Interdiscip. Rev.: Comput. Mol. Sci.*, 2012, **2**, 1–42.
76 R. F. W. Bader, *Acc. Chem. Res.*, 1985, **18**, 9–15.
77 D. D. Sung and I. Lee, *J. Phys. Chem. A*, 2011, **115**, 3386–3392.
78 Y. Ren, X.-G. Wei, S.-J. Ren, K.-C. Lau, N.-B. Wong and W.-K. Li, *J. Comput. Chem.*, 2013, **34**, 1997–2005.
79 R. Robiette, T. Trieu-Van, V. K. Aggarwal and J. N. Harvey, *J. Am. Chem. Soc.*, 2016, **138**, 734–737.
80 B. Galabov, G. Koleva, H. F. Schaefer and W. D. Allen, *Chem. – Eur. J.*, 2018, **24**, 11637–11648.
81 E. Espinosa, I. Alkorta, J. Elguero and E. Molins, *J. Chem. Phys.*, 2002, **117**, 5529–5542.
82 R. Hernández-Esparza, S.-M. Mejía-Chica, A. D. Zapata-Escobar, A. Guevara-García, A. Martínez-Melchor, J.-M. Hernández-Pérez, R. Vargas and J. Garza, *J. Comput. Chem.*, 2014, **35**, 2272–2278.
83 R. Hernández-Esparza, l Vázquez-Mayagoitia, L.-A. Soriano-Agueda, R. Vargas and J. Garza, *Int. J. Quantum Chem.*, 2019, **119**, e25671.
84 R. Vargas, J. Garza, A. Martínez and I. A. Ibarra, *Chem. Commun.*, 2024, **60**, 3008–3018.
85 T. Hansen, P. Vermeeren, M. Bickelhaupt and T. A. Hamlin, *J. Phys. Chem. B*, 2021, **60**, 20840–20848.
86 D. K. Bohme and L. B. Young, *J. Am. Chem. Soc.*, 1970, **92**, 7354–7358.
87 D. K. Bohme, G. I. Mackay and J. D. Payzant, *J. Am. Chem. Soc.*, 1974, **96**, 4027–4028.
88 G. S. Hammond, *J. Am. Chem. Soc.*, 1955, **77**, 334–338.
89 M. Fugel, A. Dittmer, F. Kleemiss and S. Grabowsky, *J. Phys. Chem. A*, 2021, **125**, 4070–4078.